CM² MAGAZINE

第 20 期

南方科技大学海洋磁学中心主编

创刊词

海洋是生命的摇篮，是文明的纽带。地球上最早的生命诞生于海洋，海洋里的生命最终进化成了人类，人类的文化融合又通过海洋得以实现。人因海而兴。

人类对海洋的探索从未停止。从远古时代美丽的神话传说，到麦哲伦的全球航行，再到现代对大洋的科学钻探计划，海洋逐渐从人类敬畏崇拜幻想的精神寄托演变成可以开发利用与科学研究的客观存在。其中，上个世纪与太空探索同步发展的大洋科学钻探计划将人类对海洋的认知推向了崭新的纬度：深海（deep sea）与深时（deep time）。大洋钻探计划让人类知道，奔流不息的大海之下，埋藏的却是亿万年的地球历史。它们记录了地球板块的运动，从而使板块构造学说得到证实；它们记录了地球环境的演变，从而让古海洋学方兴未艾。

在探索海洋的悠久历史中，从大航海时代的导航，到大洋钻探计划中不可或缺的磁性地层学，磁学发挥了不可替代的作用。这不是偶然，因为从微观到宏观，磁性是最基本的物理属性之一，可以说，万物皆有磁性。基于课题组的学科背景和对海洋的理解，我们对海洋的探索以磁学为主要手段，海洋磁学中心因此而生。

海洋磁学中心，简称 CM^2，一为其全名“Centre for Marine Magnetism”的缩写，另者恰与爱因斯坦著名的质能方程 $E = MC^2$ 对称，借以表达我们对科学巨匠的敬仰和对科学的不懈追求。

然而科学从来不是单打独斗的产物。我们以磁学为研究海洋的主攻利器，但绝不仅限于磁学。凡与磁学相关的领域均是我们关注的重点。为了跟踪反映国内外地球科学特别是与磁学有关的地球科学领域的最新研究进展，海洋磁学中心特地主办 CM^2 Magazine，以期与各位地球科学工作者相互交流学习、合作共进！

“海洋孕育了生命，联通了世界，促进了发展”。 21 世纪是海洋科学的时代，由陆向海，让我们携手迈进中国海洋科学的黄金时代

目 录

海磁快讯

刘青松教授荣升南科大讲席教授

近日，通过南方科技大学参照世界一流高校的严格国际评审，海洋磁学中心学术带头人刘青松教授荣升讲席教授。

刘青松教授于 2016 年 8 月加入南方科技大学，目前担任南科大教授会会长、海洋科学与工程系教授、党支部书记，是南科大培养的第一位教育部特聘教授。刘青松教授 2017 年获得南科大“优秀导师奖”，2018 年入选深圳市国家级领军人才，2019 年被评为深圳高校唯一入选的“全国模范教师”。2020 年 3 月，其领衔的 “远洋垂起固定翼无人机磁测系统海试成功”项目入选 2019 年中国十大海洋科技进展。

作为南科大教授会会长，刘青松教授还致力于公共教育和科普传播。他积极推动《十万个高科技为什么》的编辑工作，创立南方科普大讲坛，多次到校内校外开展科普活动。新冠肺炎疫情期间，刘青松教授除了日常的科研教育活动外，还面向全国公众讲授《青松读懂地球》的科普课，广受好评。

科研感想

王浩森

如果从硕士第一年算踏入科研行列，于今也快 3 年。

这三年中不光年龄有所增长，对于科研也有了自己的一些见解。

读博之前总觉得自己还小，知识需要老师的灌输。但是读博以后发现，老师的作用更多的，且更重要的在于引导，引导你向正确的方向越走越远。博士在科研中，学到更多的是一种思考问题的模式。“提出问题、设计实验、数据处理、写文章、改文章“等等。这种过程穿插在整个博士期间并且会影响到以后的生活。并且此过程中要与导师不断的交流进行思维的碰撞，不断与导师进行思想的交换，吸取导师思维模式来补充自身的漏洞。每当一篇文章正式投出，结束了一个周期，便会增长一些经验，经验的积累就是自身成长的过程。这个过程也就是所谓的研究。

虽然大家同在一个研究领域，但是博士同学之间的差距还是会有很大的区别，这区别取决于自身的学习主动性，自身所处环境以及前辈人的引导等等一些因素。当然最主要的还是取决于自身，因为一个人的主观能动性能够决定着未来的发展限度。不懂的问题应当主动请教他人，而不是等着他人来主动问你是否哪里不会；发现感兴趣的文章或观点也应当主动联系他人以寻求有益的讨论，这些对于自己的科研生涯来说都是大有脾益的。

当然，读博不是为了最后那一纸文凭，也不是追逐虚无的名和利。最重要的是自己在几年的训练中，能够纯粹心无旁骛的做好这件事，能够按照自己的意愿达到自己所理想的高度。

第 10 章　AMS 应用

对于 AMS 椭球，初学者最难判断的就是根据投影图来判断 AMS 的形状与方位。

我们再复习一下，如果短轴扎堆，长轴无定向，这就是一个典型的大饼状 AMS 椭球。如果长轴扎堆，短轴无定向，这就是典型的针状 AMS 椭球。

我们再来看几个复杂一点的情形。对于第一列，长轴有非常清晰的定向，而中间轴和短轴形成一个马鞍形，没有定向，所以这是一个较为典型的针状 AMS 椭球。对于第二列，短轴集中在中心（倾角为 90°），而长轴和中间轴在水平面（倾角为零）随机分布，这就是一个典型的大饼状 AMS 椭球。对于第三列，三个轴好像可以分开，这个 AMS 椭球相对模糊，属于三轴和针状 AMS 椭球过渡的情形。第四列则是典型的三轴 AMS 椭球，三个轴都非常清晰地各自扎堆。

我个人非常喜欢 T-P 图。Y 轴是形状因子 T，$T = 0$ 代表着三轴椭球，$T > 0$ 代表着大饼状椭球，$T < 0$ 则代表着针状椭球。非常清晰，一路了然。

X 轴则是各向异性度 P，比如在针状椭球区，P 越大，表示越拉长。

当 P 较小时，AMS 椭球是针状，可是随着 P 的增大，AMS 椭球的形状逐渐向大饼状转化。可以想象一种情形，我们把一个橄榄球沿着长轴进行压缩，慢慢地就会把这个拉长的形状压成一个大饼。

可见这种 T-P 图可以很好地展示 AMS 变化的动态过程。

在自然界中，PSD/MD 颗粒在沉积的时候都喜欢把长轴放在水平面上，短轴在垂直面上。比如，你手中有一个烧饼，掉落在地上，肯定是长轴水平放置。这就会形成一个最为典型的大饼状沉积磁组构。此时 K1 的倾角很小，而 K3 的倾角则接近垂直。

要是 K1 的倾角变为高角度，比如 80°，这代表着什么？

一般情况下，这代表沉积物后期可能受到了较为强烈的扰动。这个性质非常有用，是我们判断沉积物受到扰动的强有力证据之一。

初学者还经常会区分不清楚 AMS 长轴的倾角和古地磁剩磁的倾角，认为二者应该一一对应才对。我们在这里重点强调一下，这两个方向完全不同，没有必然的联系。别忘记了，M 和颗粒物理长轴之间是可以有夹角的。

可是如果我们同时测量一个剖面的 AMS 长轴与短轴的倾角和古地磁倾角，就可以判断古地磁的倾角异常是扰动造成的还是真正的地磁事件。比如，我们把这种研究思路应用于中国黄土。中国黄土确实能够记录一些古地磁事件，但是也常常受到各种扰动形成古地磁倾角异常。如果古地磁倾角异常对应着 AMS 长轴高角度异常，这就说明前者可能受到了地层扰动的影响，而不是真正的古地磁事件。

上面提及长轴 K1 和短轴 K3 的倾角应用。K1 的偏角（K1-Dec）有什么用处吗？

K1-Dec 的用处更大，因为它代表着受到某种地质作用进行了定向排列。对于河流沉积物，K1-Dec 可能代表着河流的方向；对于中国黄土，K1-Dec 可能代表着冬季风的方向；对于熔岩流，K1-Dec 可能代表着熔岩流的流动方向。

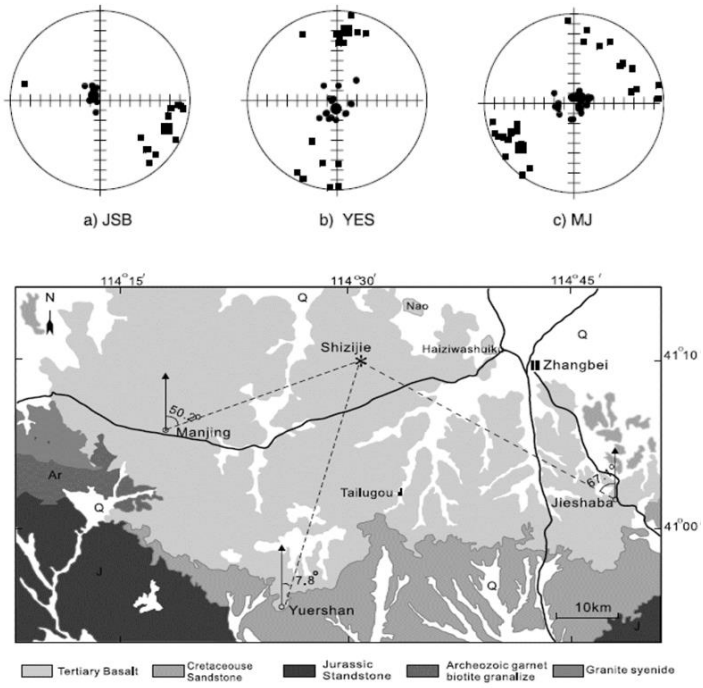

图 1 通过 AMS 寻找火山喷发口（Zhu et al., GRL, 2003）

我们来看一个教科书级别的例子。早期火山喷发留下的火山口早已被后来的植被和地层覆盖。我们在该区不同的地方可以找到熔岩流。于是，定向采集这些零零散散的熔岩流标本，测量它们的 AMS 参数。可见，在 MJ 剖面，K1-Dec 指向东北-西南；在 YES 剖面，K1-Dec 则稍微指向北偏东-南偏西；而在 JSB 剖面，K1-Dec 则指向东偏南-西偏北。我们把这些方向投影到地图上，三者的交点就确定了火山口的位置。

我们必须指出，熔岩流在流动过程中确实能够把磁性颗粒沿着熔岩流的方向定向排列。但是在熔岩流的边部和最前端，熔岩流会向下流动，此时 AMS 的结果会凌乱。

当原始的大饼状磁组构受到后期构造应力作用时，在 T-P 图上会表现出系统的变化。比如，T 和 P 先减小，然后再变大。这种模式可以被用来指示构造应力影响。

文献导读

1. 末次冰消期硅循环的深水翻转和重组特性

翻译人：仲义 zhongy@sustech.edu.cn

M. Dumont, L. Oichevin, W.Geibert, et al., ***The nature of deep overturning and reconfigurations of the silicon cycle across the last deglaciation*** *[J]. Nature Communication, 2020, 11(1), 1534. Doi: 10.1038/s41467-020-15101-6.*

摘要：海洋环流的改变和生物碳泵被认为是驱动末次冰消期大气 CO_2 升高的主要因素；然而其背后的过程还存在不一致性。过去的记录已经暗示了在大气 CO_2 上升的两个阶段为深水环流通风作用的划分，但是不同的通风状态对 Si 循环过程还没有进行探讨。本文中基于南大洋海洋沉积物中的硅藻和海绵骨针的 Si 同位素记录综合反映出 Si 同位素的在冰消期明显升高，并在新仙女木事件时期（YD）达到最高值。我们认为南极海冰和大西洋翻转流的变化促进了 YD 时期海底深水通风作用，并导致 Si 循环发生重组。通过调节生物泵的强度，Si 循环在冰期-间冰期的移动对晚更新世 CO_2 浓度变化起到重要作用。

ABSTRACT: Changes in ocean circulation and the biological carbon pump have been implicated as the drivers behind the rise in atmospheric CO_2 across the last deglaciation; however, the processes involved remain uncertain. Previous records have hinted at a partitioning of deep ocean ventilation across the two major intervals of atmospheric CO_2 rise, but the consequences of differential ventilation on the Si cycle has not been explored. Here we present three new records of silicon isotopes in diatoms and sponges from the Southern Ocean that together show increased Si supply from deep mixing during the deglaciation with a maximum during the Younger Dryas (YD). We suggest Antarctic sea ice and Atlantic overturning conditions favoured abyssal ocean ventilation at the YD and marked an interval of Si cycle reorganisation. By regulating the strength of the biological pump, the glacial–interglacial shift in the Si cycle may present an important control on Pleistocene CO_2 concentrations.

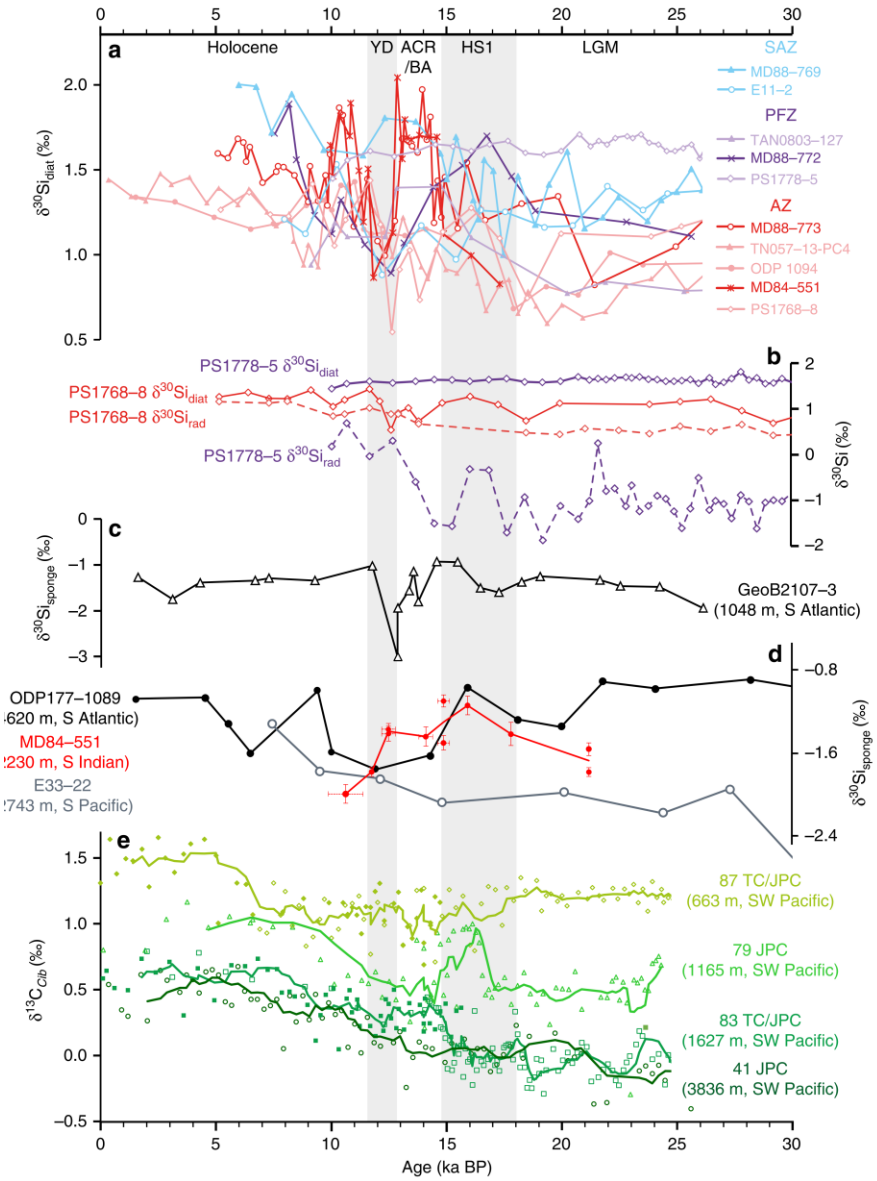

Figure 1. A global compilation of silicon isotope data demonstrating the reorganisation of the DSi distribution across the last deglaciation. a Diatom silicon isotope (δ^{30}Sidiat) records from the Antarctic Zone (red), Polar Front Zone (purple) and Subantarctic Zone (blue). MD88-769. E11-2 & ODP1094. TAN0803-127. PS1778-5 & PS1768-8. TN057-13-PC4. b Diatom (δ^{30}Sidiat) and radiolarian (δ^{30}Sirad) silicon isotope records from PS1768-8 and PS1778-5 in the Atlantic sector reconstructing changes in the vertical DSi gradient in the upper Southern Ocean. c A sponge silicon isotope record (δ^{30}Sisponge) from 1048 m in the South Atlantic recording changes in DSi content within intermediate waters. d δ^{30}Sisponge record from MD84-551 accompanied by records from the south Atlantic and south Pacific. Vertical error bars display ±1SE. Horizontal error bars, where present, represent the age range of the samples used to produce the given data point. Together these δ^{30}Sisponge records demonstrate the deglacial changes in deep ocean DSi gradients. e Four benthic foraminiferal (Cibicidoides wuellerstorfi) δ^{13}C records from the southwest Pacific highlighting the timing of ventilation changes in the Pacific across the last deglaciation. Solid and open symbols represent samples from jumbo piston and trigger cores, respectively.

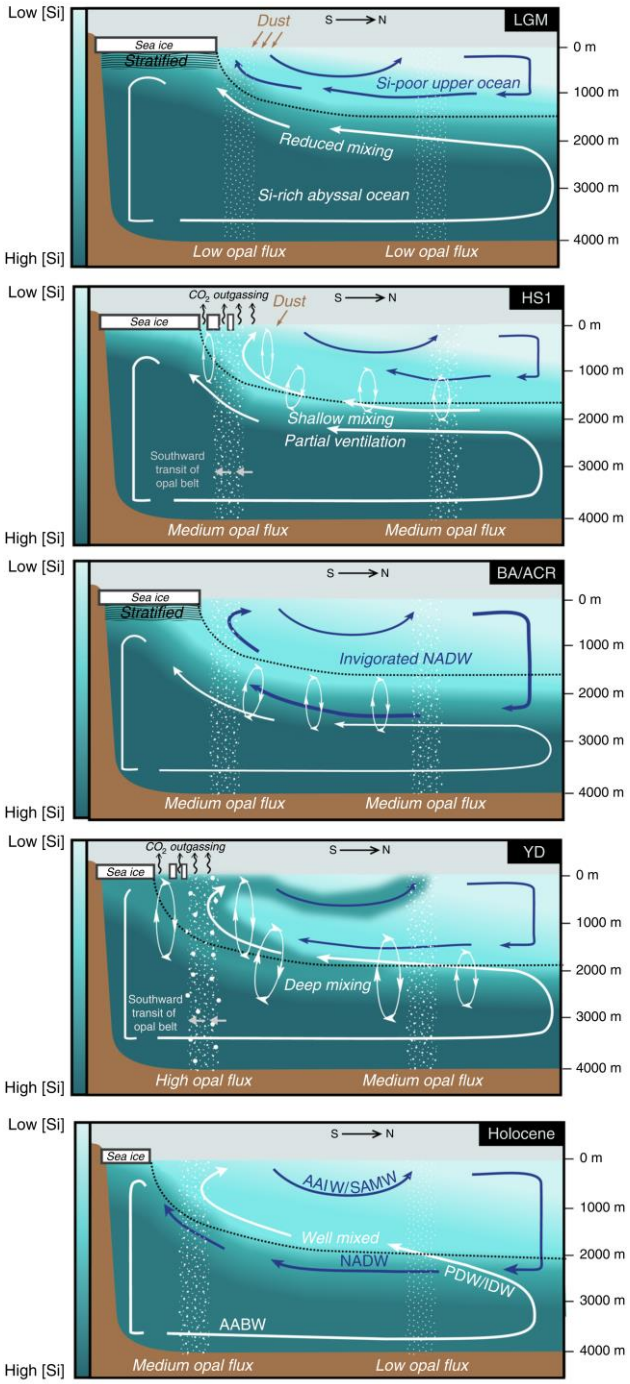

Figure 2. A schematic representation of the circulation changes and concomitant DSi distribution across the deglaciation. In each panel the upper (NADW/AAIW/SAMW) and lower (AABW/PDW/IDW) circulatory cells are depicted as blue and white arrows, respectively. The shading in each panel represents the concentration of DSi, with the LGM abyssal ocean being more DSi-rich than the modern as a result of reduced mixing. The dotted black line in each of the panels represents the isopycnal at divergence of the upper and lower circulatory cells, the vertical position of which has been suggested to be governed by sea ice extent. Importantly, this schematic demonstrates that only when sea ice is sufficiently removed during the Younger Dryas are the deep Si-rich waters tapped into and redistributed into the upper circulatory cell. Southern Ocean and low latitude opal fluxes are globally generalised based on available data.

2. 大洋地幔柱的记录证明了超大陆-地幔柱事件存在耦合

翻译人：冯婉仪 fengwy@sustech.edu.cn

Doucet L S, Li Z X, Ernst R E, et al. ***Coupled supercontinent–mantle plume events evidenced by oceanic plume record****[J].* ***Geology****, 2020. https:// doi.org/10.1130/G46754.1.*

摘要：现今下地幔最主要的特征是非洲和太平洋两个对跖的大型低剪切速率省（LLSVPs）。这两个结构是如何形成的，何时形成的，在地球历史中，它们是固定的且存在了很长时间，还是动态的并与超大陆的周期有关，仍然是一阶地球动力学问题。热点和大火成岩省（LIPs）大多数产生于 LLSVPs 之上，并且人们普遍认为非洲 LLSVP 至少在~ 200 Ma 前存在于泛古陆之下。虽然大陆 LIP 的记录被用来解释在大陆之下的地幔柱活动的空间和时间变化，但在 ~ 170 Ma 之前的海洋中的地幔柱记录大多由于洋壳俯冲而丢失。在这里，我们展示了第一个大洋大火成岩省数据库（O-LIPdb）的编译，它代表了保存的大洋 LIP 和在蛇绿岩中的保存的洋岛玄武岩。利用这个数据库，我们可以重建和比较过去 20 亿年间（跨越三个超大陆旋回）在大陆和海洋中地幔柱活动的记录。时间序列分析揭示了在大陆和海洋中的地幔柱活动具有相似的周期性，两者都显示出一个~ 500 Ma 的周期性，这与超大陆的周期相当，尽管有轻微的相位延迟。我们的研究结果证明了 LLSVPs 是动态的，其中超大陆的周期和全球俯冲带的几何结构控制着地幔柱的形成和位置。

ABSTRACT: The most dominant features in the present-day lower mantle are the two antipodal African and Pacific large low-shear-velocity provinces (LLSVPs). How and when these two structures formed, and whether they are fixed and long lived through Earth history or dynamic and linked to the supercontinent cycles, remain first-order geodynamic questions. Hotspots and large igneous provinces (LIPs) are mostly generated above LLSVPs, and it is widely accepted that the African LLSVP existed by at least ca. 200 Ma beneath the supercontinent Pangea. Whereas the continental LIP record has been used to decipher the spatial and temporal variations of plume activity under the continents, plume records of the oceanic realm before ca. 170 Ma are mostly missing due to oceanic subduction. Here, we present the first compilation of an Oceanic Large Igneous Provinces database (O-LIPdb), which represents the preserved oceanic LIP and oceanic island basalt occurrences preserved in ophiolites. Using this database, we are able to reconstruct and

compare the record of mantle plume activity in both the continental and oceanic realms for the past 2 b.y., spanning three supercontinent cycles. Time-series analysis reveals hints of similar cyclicity of the plume activity in the continent and oceanic realms, both exhibiting a periodicity of ~500 m.y. that is comparable to the supercontinent cycle, albeit with a slight phase delay. Our results argue for dynamic LLSVPs where the supercontinent cycle and global subduction geometry control the formation and locations of the plumes.

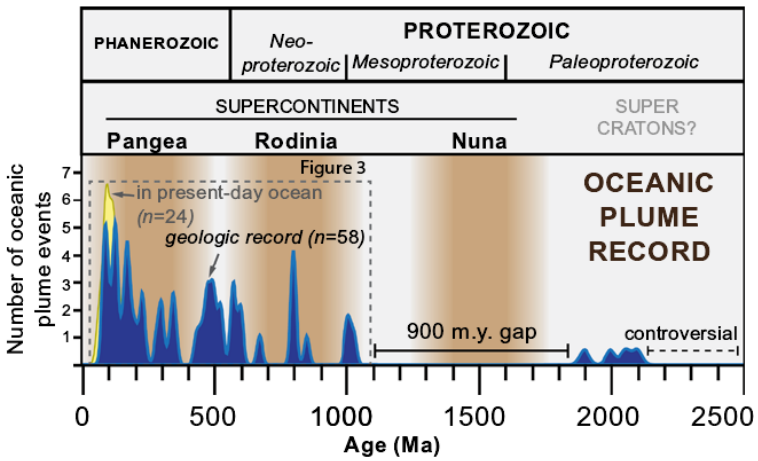

Figure 1. Age distribution of oceanic mantle plume occurrences for the past 2500 m.y. plotted against known supercontinents. Note that Gondwana is not considered a true supercontinent here because it consists of only half of all continents at the time, and is therefore regarded as an intermediate stage during the assembly of the true supercontinent Pangea (Evans et al., 2016). The ophiolitic nature of Archean greenstone belts remains controversial.

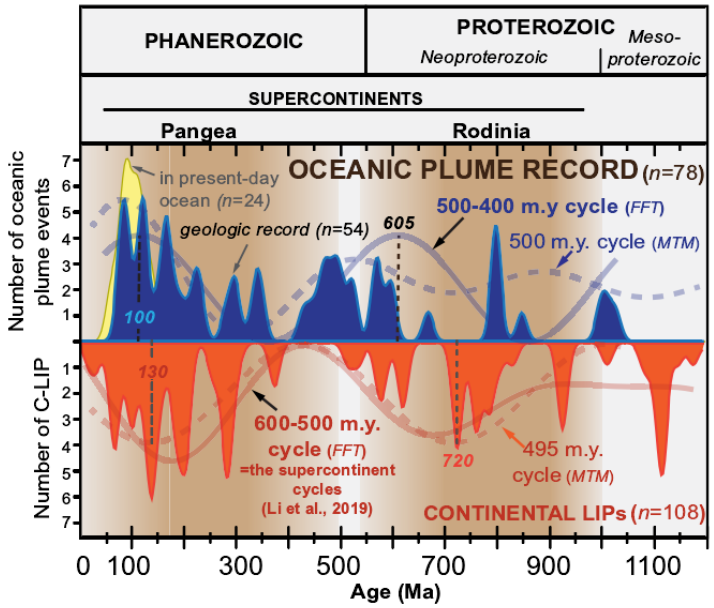

Figure 2. Distribution of both oceanic (blue) and continental (red) mantle plume occurrences for the past 1200 m.y., plotted against the life cycles of supercontinents Rodinia and Pangea, and time-series analyses (fast-Fourier transform [FFT] and multi-taper method [MTM]) of both continental and oceanic large igneous province (C-LIP and O-LIP, respectively) records (see text, and Data Repository figures [see

footnote 1] for details).

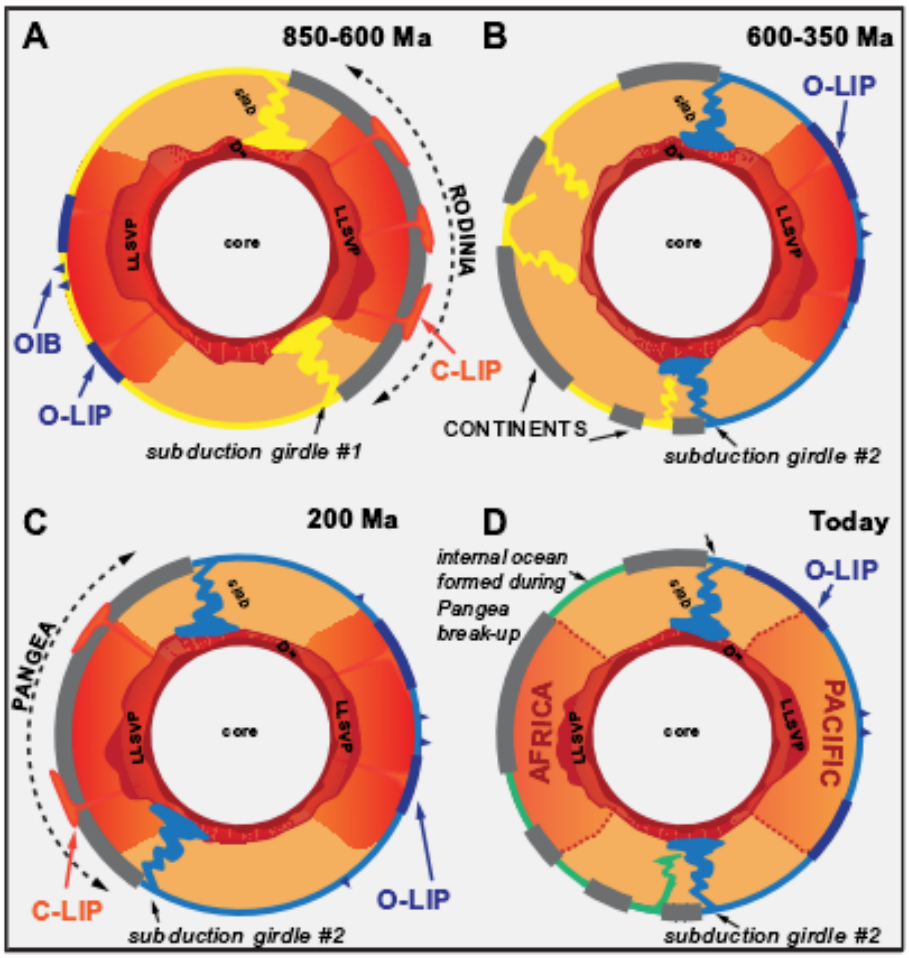

Figure 3. Cartoon of dynamic and coupled supercontinent-plume cycles model (after Li et al., 2019). (A) 850- 600 Ma, formation of antipodal large low-shear-velocity provinces (LLSVPs) (and mantle plumes above them) by the circum-Rodinia subduction girdle (yellow) after Rodinia's final assembly at 900 Ma (Li et al., 2004, 2008). "D" marks the lowermost portion of the mantle, at the core-mantle boundary. (B) 600-350 Ma, the protracted and complete breakup of Rodinia, where Rodinia LLSVP (by now under the paleo-Pacific ocean) was still active while Gondwana and Pangea started to assemble above the vanishing antipodal oceanic LLSVP. (C) 200 Ma, formation of antipodal LLSVPs by the circum-Pangea subduction girdle (blue) after Pangea's final assembly at 320 Ma. (D) Present-day configuration of residual antipodal, equatorial African and Pacific LLSVPs after Pangea breakup, but before the assembly of the future supercontinent. O-LIP—oceanic large igneous province; C-LIP—continental large igneous province; OIB—oceanic island basalt.

3. 2018 年极端降雨触发基拉韦厄火山喷发

翻译人：蒋晓东 jiangxd@sustech.edu.cn

Farquharson, J.I., Amelung, F. 2020. ***Extreme rainfall triggered the 2018 rift eruption at Kīlauea Volcano*** *[J] (2020).Nature, 580, 491-495.*

摘要：2018 年 5 月夏威夷基拉韦厄火山喷发是过去至少 200 年里非常特别的喷发事件，然而它的触发机制仍然未知。这次事件之前出现了几个月异常高的沉积。先前有观点认为降雨能够调节浅层的火山活动，但是否能影响深部岩浆传输仍不清楚。本研究揭示在基拉韦厄火山喷发前和喷发期间，降雨渗透到火山底部使得深度 1-3 公里处的孔隙压强从 0.1 升高到 1 千帕，并且达到了过去 50 年的最高值。本研究认为裂隙区域的孔隙压力改变而弱化或者破坏了火山底下的物质结构，触发了岩浆侵入和火山喷发。沉积诱导的喷发机制与先兆缺失的膨胀峰值表明，此次喷发并不是因新岩浆侵入裂缝区引起。此外，历史喷发事件统计分析的结果表明降雨模式对基拉韦厄火山喷发的时长与频率具有实质性的贡献。因此，火山活动可以被极端降雨调节，即降雨触发岩石破坏，这也是评估火山灾害必须考虑的一个因素。值得注意的是，人类活动引起的气候变化及日渐增多的极端天气可以增加降雨触发全球范围内火山喷发的可能性

ABSTRACT：The May 2018 rift intrusion and eruption of Kīlauea Volcano, Hawai‘i, represented one of its most extraordinary eruptive sequences in at least 200 years, yet the trigger mechanism remains elusive1. The event was preceded by several months of anomalously high precipitation. It has been proposed that rainfall can modulate shallow volcanic activity, but it remains unknown whether it can have impacts at the greater depths associated with magma transport. Here we show that immediately before and during the eruption, infiltration of rainfall into Kīlauea Volcano’s subsurface increased pore pressure at depths of 1 to 3 kilometres by 0.1 to 1 kilopascals, to its highest pressure in almost 50 years. We propose that weakening and mechanical failure of the edifice was driven by changes in pore pressure within the rift zone, prompting opportunistic dyke intrusion and ultimately facilitating the eruption. A precipitation-induced eruption trigger is consistent with the lack of precursory summit inflation, showing that this intrusion—unlike others—was not caused by the forceful intrusion of new magma into the rift zone. Moreover, statistical analysis of historic eruption occurrence suggests that rainfall patterns

contribute substantially to the timing and frequency of Kīlauea's eruptions and intrusions. Thus, volcanic activity can be modulated by extreme rainfall triggering edifice rock failure—a factor that should be considered when assessing volcanic hazards. Notably, the increasingly extreme weather patterns associated with ongoing anthropogenic climate change could increase the potential for rainfall-triggered volcanic phenomena worldwide.

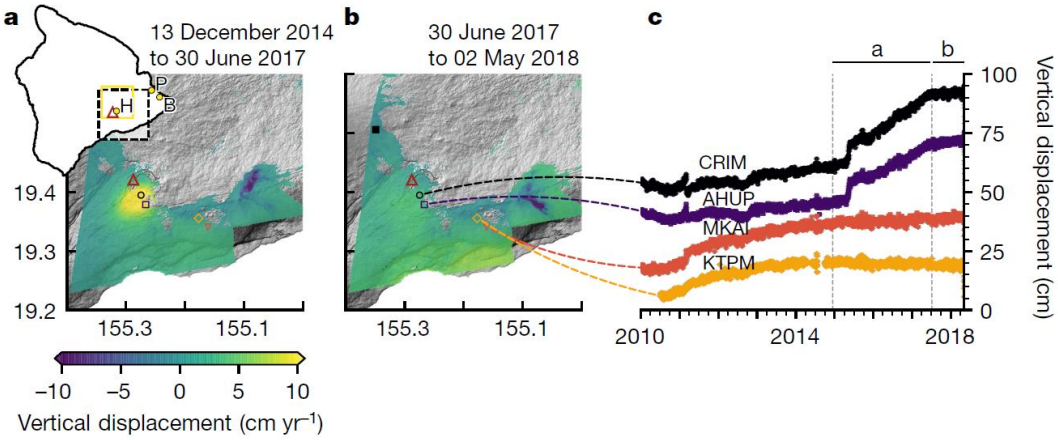

Figure 1. Pre-eruption ground deformation of the study site. **a**, Vertical deformation map derived from Sentinel-1 InSAR data (ascending track 124 and descending track 87) between December 2014 and June 2017. Inset, map showing the location of Kīlauea Volcano (red triangle) and the HVNP rain gauge (H) within the Eastern Rift Zone. The yellow box outlines the 0.25° × 0.25° TRMM/GPM footprint used here. The Paradise Park well (P) and Hawaiian Beaches rain gauge (B) are also highlighted (see Extended Data Fig. 1). The dashed box indicates the region shown in **a**, **b**. In **b**, the filled square is a reference point; in a, b, open symbols represent GPS station locations. b, Vertical deformation between June 2017 and May 2018. **c**, Vertical GPS displacement of the Kīlauea flank from 2010. Station names are shown on the panel; colours correspond to locations in **a**, **b**. Dashed vertical lines highlight marked changes-of-slope in station data proximal to the summit (for CRIM and AHUP). Datasets have been offset from the x axis for clarity.

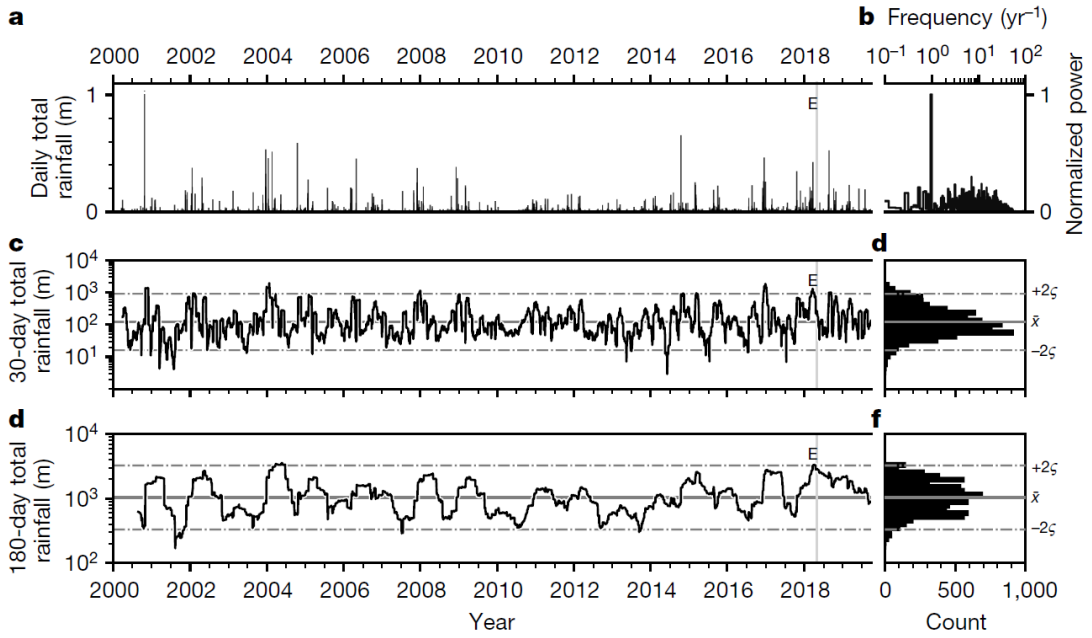

Figure 2. Rainfall over Kīlauea. **a**, Calibrated daily rainfall amount over Kīlauea from March 2000 to July 2019 (TRMM/GPM data calibrated with gauge data; see Fig. 1a inset and Methods). The vertical bar shows the date of flank eruption (E). **b**, Power spectrum of Fourier-transformed rainfall time series (a) shown in the (normalized) power–frequency domain. **c**, Rolling 30-day cumulative rainfall since March 2000 at Kīlauea. Horizontal dashed lines delineate two standard deviations either side of the mean (x±ς). **d**, Histogram of data in c on log-linear axes. **e**, Rolling 180-day cumulative rainfall. **f**, Histogram of data from e on log-linear axes.

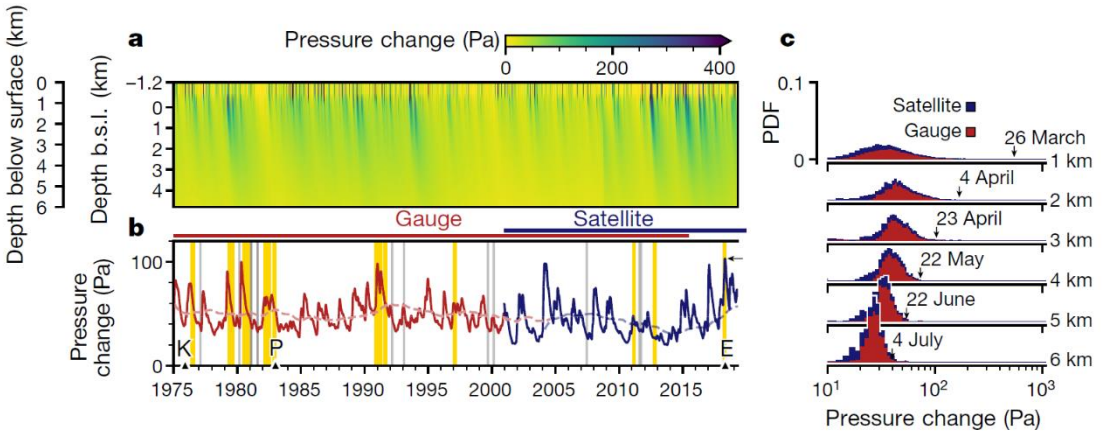

Figure 3. Pore-pressure change in response to infiltration into Kīlauea's edifice. **a**, Pore-pressure change modelled over the period January 1975 to April 2019, using available HVNP gauge data (1950-2015) and calibrated satellite data (2000-2019), with depth and time. Daily rainfall data are used as a fluctuating boundary condition. Colour scale indicates pressure change. **b**, Pore-pressure change at 3 km below the surface (1.8 km b.s.l.) modelled over the period January 1950 to April 2019 (data shown are since the 1975 Kalapana earthquake). The dashed line shows the four-year running average. K represents the 1975 magnitude-7.2 Kalapana earthquake; P shows the 1983 onset of the Pu'u 'Ō'ō eruption; E represents the 2018 Kīlauea rift intrusion-eruption. Vertical bars show reported intrusion events within the rift zone, after refs. 22,26-28. Intrusions are highlighted in

yellow if they coincide with periods during which pressure change exceeds the four-year average, and grey if they do not. Intrusion 33 in this time series corresponds to the early 2018 activity (intrusion detected mid- March, followed by the rift eruption on 3 May). The arrow highlights the maximum pore-pressure perturbation over this timeframe (1975 to 2019), coinciding with the onset of 2018's rift eruption. Horizontal bars indicate data availability. **c**, Probability density function (PDF) of modelled pressure change at depths 1-6 km below the surface. Arrows highlight the pore-pressure front diffusing from near the surface (1 km) to greater depths over time (26 March, 4 April, 23 April, 22 May, 22 June and 4 July 2018 at 1 km, 2 km, 3 km, 4 km, 5 km and 6 km below surface).

4. 熔结凝灰岩的古强度估计：对 Bishop Tuff 的修改

翻译人：李园洁 liyj3@sustech.edu.cn

Avery M S, Gee J S, Bowles J A, et al. ***Paleointensity estimates from ignimbrites: The Bishop Tuff revisited[J]. Geochemistry, Geophysics, Geosystems****, 2018, 19(10): 3811-3831.*

摘要：火山灰流凝灰岩（熔结凝灰岩）可能含有单畴大小的（钛铁矿）磁铁矿，应能很好地记录地磁场强度，但由于它们的复杂的热历史，还含有其他磁性颗粒，这些磁性颗粒会使古强度的确定变得复杂。对∽767 ka Bishop Tuff 是否适用于测量古强度的初步研究发现，估计值为 43.0±3.2μT。这项初步研究还表明，在可靠的古强度估计中存在空间各项异性，这可能与气相变化和火山喷气活动有关，因此需要对 Bishop Tuff 重新采样来研究磁学性质的空间变化。我们在欧文斯河峡谷内的三个新 Bishop Tuff 地层剖面上采样，并重新解释了该地区的初始研究的古强度结果。所有位点的平均值为 41.9±11.8μT；这与最初的研究结果是一致的，但分散性更大。两个剖面有气相变化的证据，存在可能携带热化学剩磁的钛赤铁矿。剖面上部的这种热化学剩磁具有高质量的古强度估计值，其强度明显高于其余部分。我们对古强度的最佳估计是 39.6±9.9μT，主要来自上部高于磁铁矿的居里温度以上的密集排列的熔结凝灰岩。低渗透性可能使它免受气相变化的影响。我们的结果表明，在解释来自凝灰岩的古强度数据时必须小心，因为可能存在非热剩磁。

ABSTRACT： Volcanic ash flow tuffs (ignimbrites) may contain single domain sized (titano)magnetite that should be good for recording geomagnetic field intensity, but due to their complex thermal histories also contain other magnetic grains which can complicate and obscure paleointensity determination. An initial study of the suitability of the ~767 ka Bishop Tuff for measuring paleointensity found an internally consistent estimate of 43.0 ± 3.2 μT. This initial study also showed a spatial heterogeneity in reliable paleointensity estimates that is possibly associated with vapor-phase alteration and fumarolic activity, which motivated resampling of the Bishop Tuff to examine spatial changes in magnetic properties. Three new stratigraphic sections of the Bishop Tuff within the Owens River gorge were sampled, and the paleointensity results from the initial study in the same locality were reinterpreted. The mean of all sites is 41.9 ±11.8 μT; this agrees with the initial study's finding but with substantially greater scatter. Two sections show evidence of

vapor-phase alteration where the presence of titanohematite, likely carrying a thermochemical remanence, produces non-ideal behavior. This thermochemical remanence in the upper portion of the section also produces some paleointensity estimates of technically high quality that have significantly higher intensity than the rest of the tuff. Our best estimate for paleointensity, 39.6 ± 9.9 μT, comes from the densely welded ignimbrite that was emplaced above the Curie temperature of magnetite. The low permeability of this unit likely shielded it from vapor-phase alteration. Our results suggest that care must be taken in interpreting paleointensity data from large tuffs as non-thermal remanence may be present.

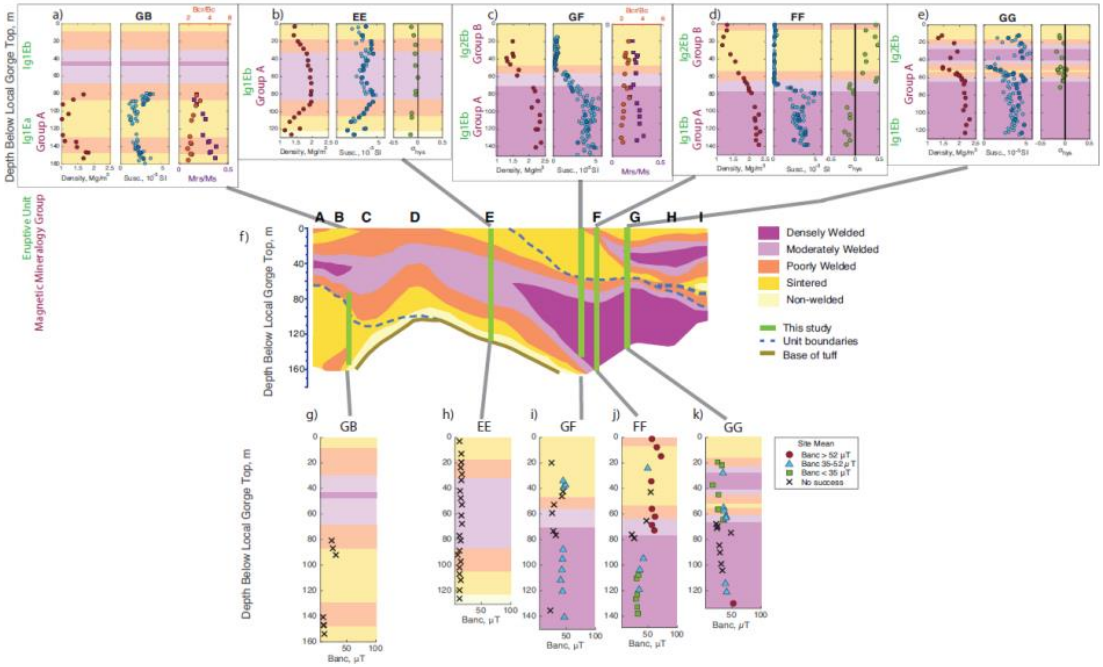

Figure 1. Summary of welding, density, magnetic properties, and B_{anc} estimates as functions of stratigraphic depth. Panels a-e) show density, magnetic susceptibility, and σ_{hys} for each section. f) Profile of degree of welding of the Bishop Tuff along the Owens River gorge. Modified from Wilson and Hildreth [2003]. g-k) Paleointensity results divided into subgroups: Type 1 B_{anc} <35 μT (red circle), Type 2 B_{anc} =35-52 μT (blue triangle), and Type 3 B_{anc} >50 μT (green square). Black x's indicate sites with no passing paleointensity data, plotted at the site mean of paleointensity estimated using the all temperature steps.

5. 古珠江的形成演化及其对南海北部源区的影响

翻译人：刘伟 inewway@163.com

Ma M, Chen G, Lyu C, et al. ***The formation and evolution of the paleo-Pearl River and its influence on the source of the northern South China sea****[J].* ***Marine and Petroleum Geology****, 2019: 171-189.*

摘要：古珠江被认为是南海北部的主要源区之一，其源头在青藏高原腹地，流经华南地块，最终流入南海珠江河口盆地(PRMB)。然而，古珠江流域的演化历史仍然是一个有争议的问题。利用南海珠江口盆地自始新世至中新世的碎屑锆石、微量元素、Nd-Sr 同位素和粘土矿物，研究了珠江口盆地沉积物的物源，重建了古珠江口盆地的水系历史。样品的 Eu/Eu、La/Sc、La/Co、Th/Sc、Th/Co、Hf-La/Th 分布图、La/Sc-Co/Th 分布图以及球粒陨石归一化稀土元素分布图表明如下结论。始新世至中新世沉积物主要来源于长英质源岩。下始新世沉积物主要由盆内隆起带提供。自上始新世以来，东江（Hongshui River）和北江（Bei River）为珠I坳陷提供了大量的长英质碎屑，并在上渐新世向珠II坳陷输送了大量的沉积物。沉积物的 Nd-Sr 同位素表明，柳江（Liu River）可能没有为珠江河口盆地提供沉积物，桂江（Gui River）可能贡献很小。沉积物的 Nd-Sr 同位素也表明，古珠江在渐新世晚期开始向西延伸，形成西江（Xi River），最终形成红水河（Hongshui River）。样品的微量元素比值也表明中新世沉积物可能从中间岩区获得了较多的输入，说明在此期间主要的物源由华南海岸向北方迁移。样品的锆石 U-Pb 年龄、Nd-Sr 同位素和粘土矿物资料支持了这一结论，表明古珠江沉积物的物源在中新世中期发生了突变。青藏高原东南部在中中新世经历了快速隆升和侵蚀作用，导致珠江水系向内陆的溯源侵蚀。

ABSTRACT: The paleo-Pearl River has been suggested as one of the major source terrains for the northern South China Sea, which headstreams in the hinterland of the Tibetan Plateau and flows through the South China Block, eventually discharges into the Pearl River Mouth Basin (PRMB) of the South China Sea (SCS). However, the drainage history of the paleo-Pearl River remains a matter of debate. Detrital zircon U-Pb ages, trace elements, Nd and Sr isotopes and clay minerals from the Eocene to Miocene sediments in the Pearl River Mouth Basin of the South China Sea have been used to investigate the sedimentary provenance and reconstruct the drainage history of the paleo-Pearl River. The Eu/Eu*, La/Sc, La/Co, Th/Sc and Th/Co ratios, the HfLa/Th and La/Sc-Co/Th

diagrams, and the chondrite normalized REE patterns of the samples suggested that the Eocene to Miocene sediments were mainly derived from felsic source rock. The Lower Eocene sediments were mainly provided by the intrabasinal uplift regions. The Dong River and Bei River initiated since Upper Eocene supplied large amounts of felsic detritus from the Southern China Coast to Zhu I Depression, and then transported sediments into the Zhu II depression during the upper Early Oligocene. The Nd and Sr isotopes of the sediments suggested that the Liu River may not provide sediments for the PRMB, however, the Gui River may have made a very small contribution. The Nd and Sr isotopes of the sediments also suggested that the paleo-Pearl River began to extend westward to form Xi River and eventually the Hongshui River in the Late Oligocene. The trace element ratios of the samples also suggested that the Miocene sediments may have received more input from an intermediate rock area, indicating the main provenance switch from the coast of South China to a northern source during this time. This conclusion has been supported by the detrital zircon U-Pb ages, Nd and Sr isotopes and clay minerals data of the samples, which show that the provenance of the sediments supplied by the paleo-Pearl River had an abrupt shift in the Middle Miocene. The southeastern Tibetan Plateau rapid uplifted and experienced erosion in the Middle Miocene, leading to the progressive headward erosion of the Pearl River system into the continental interior.

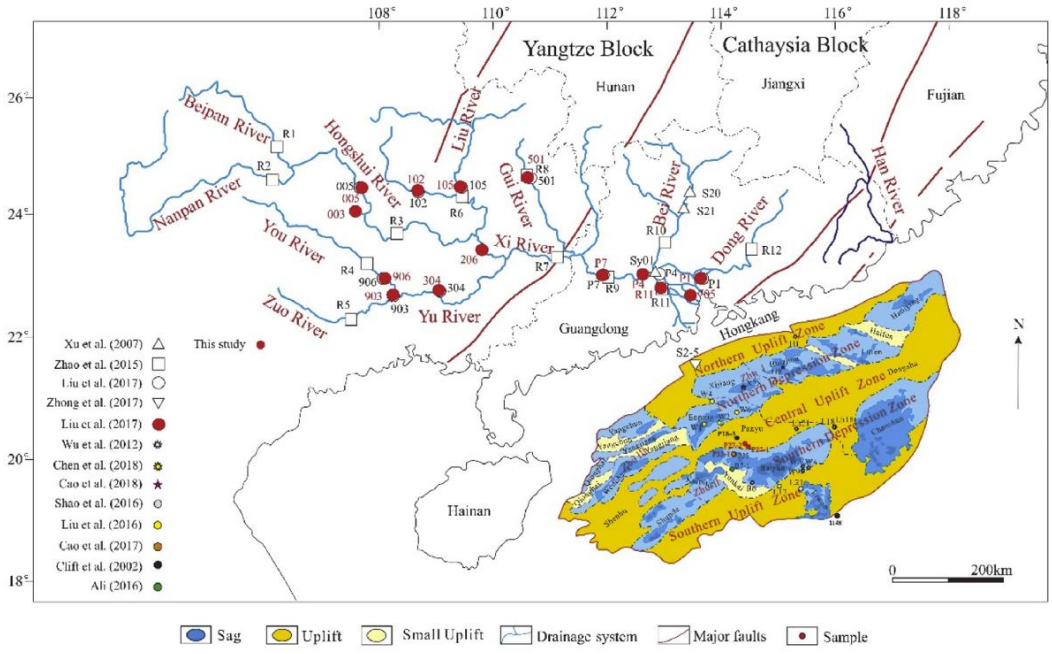

Figure 1. The major structural and tectonic elements of the SCB and PRMB, the distribution of the modern Pearl River tributaries and the sampling locations (Modified
after Liu et al., 2017; Wang et al., 2017 and Cao et al., 2018).

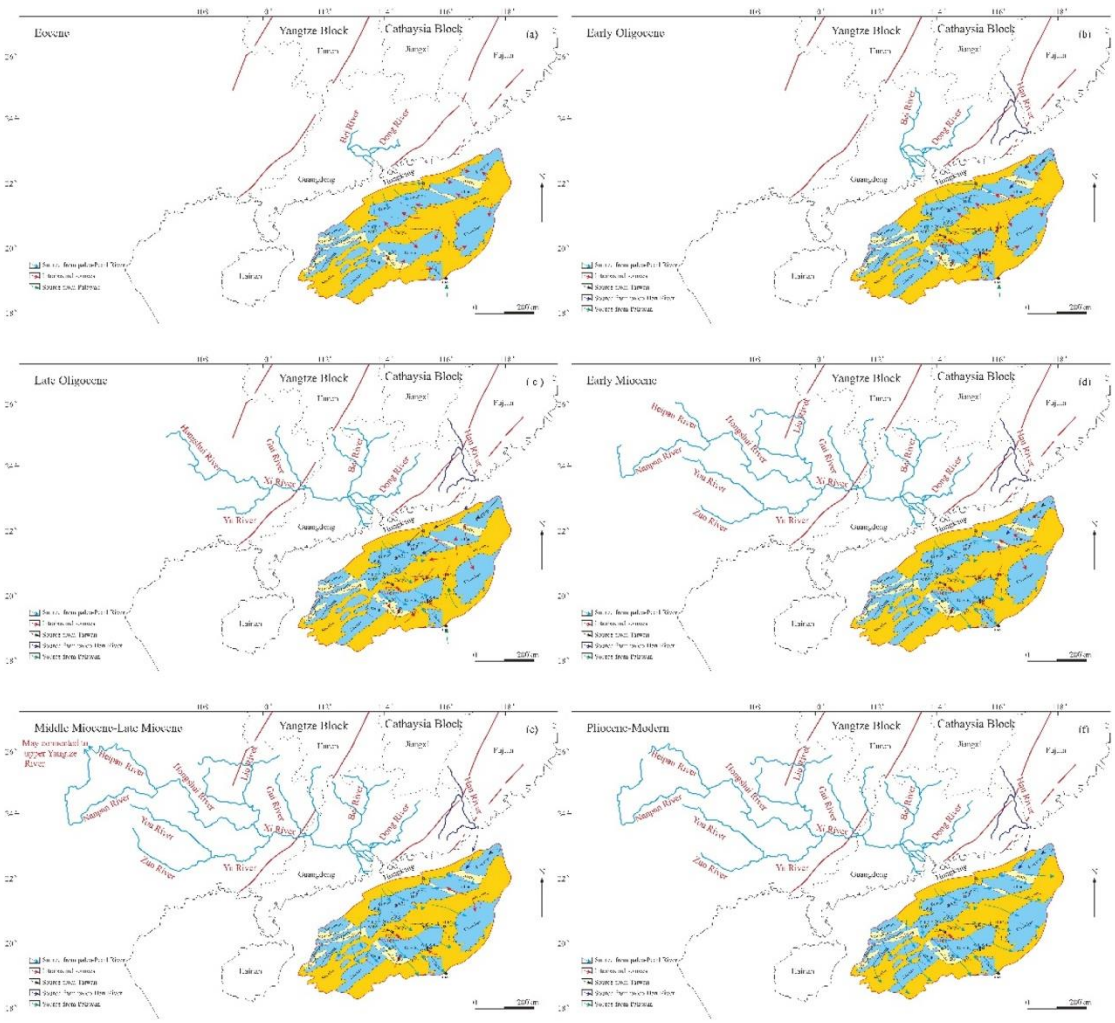

Figure 2. Schematic reconstructions for the Eocene-Pliocene drainage history of the paleo-Pearl River and the provenance evolution of the PRMB. The arrow shows generalized provenance directions.

6. 中国石笋氧同位素仅由印度夏季风控制吗？

翻译人：杨会会 11849590@mail.sustech.edu.cn

Li D, Tan L C, Cai Y J, et al. ***Is Chinese stalagmite $\delta^{18}O$ solely controlled by the Indian summer monsoon? [J]. Climate Dynamics*** *,2019,53:2969–2983*

摘要：石笋作为一种独特的陆地地质档案，在重建古气候变化方面得到了广泛的应用。然而，对中国石笋 $\delta^{18}O$ 的解译仍然具有争议。最近，Community Atmosphere Model 版本 3（CAM3）的研究表明，在 Heinrich 事件期间，中国东部石笋的 $\delta^{18}O$ 揭示的是印度夏季风（ISM）强度，而非东亚夏季风（EASM）强度。本文展示了山西省降龙洞石笋 $\delta^{18}O$ 在 25.5-10.9 ka 的高分辨率记录。XL15 的 $\delta^{18}O$ 记录显示，格陵兰冰芯记录与中国和印度的其他气候记录在千年尺度上具有相似变化，包括 H2,H1,BA 和 YD 事件，支持亚洲季风和北半球高纬气候之间的联系。此外，中国东部和印度夏季风区的石笋 $\delta^{18}O$ 的在冰期-间冰期尺度和十年际尺度的区别也被发现。这意味着印度夏季风不是 H 事件期间中国石笋 $\delta^{18}O$ 的单一控制因素。当从 XL15 的 $\delta^{18}O$ 中减去印度石笋的 $\delta^{18}O$ 之后，我们发现 XL15 的记录与西太平洋暖池的海表温度呈明显的负相关。结果，我们的研究表明中国石笋 $\delta^{18}O$ 在轨道尺度，千年尺度和十年际尺度上都由印度夏季风和东亚夏季风共同控制。

ABSTRACT: As a unique continental archive, speleothem has been widely used in reconstructing paleoclimate change. However, the interpretation of Chinese speleothems $\delta^{18}O$ has remained a subject of debate. Recently, a Community Atmosphere Model version 3 (CAM3) study indicated that the stalagmite $\delta^{18}O$ from eastern China reflected the Indian summer monsoon (ISM) intensity rather than the East Asian summer monsoon (EASM) intensity during Heinrich events. Here, we present a high resolution speleothem $\delta^{18}O$ record from Xianglong Cave in Shanxi province, China, covering the period of 25.5–10.9 ka BP. The XL15 record shows similar variations with ice core record from Greenland and other climate records from China and India on millennial scale, including Heinrich 2 (H2), Heinrich 1 (H1), Bølling–Allerød (BA) and Younger Dryas (YD) events, supporting the connection between the Asian monsoon and northern high latitude climate. The $\delta^{18}O$ amplitude of our record is larger than or similar to the stalagmite $\delta^{18}O$ records from India during these events. In addition, differences of stalagmite $\delta^{18}O$ in eastern China and the ISM region were observed on glacial-interglacial as well as

decadal timescales. That means the ISM is not the sole controlling factor of Chinese stalagmite $\delta^{18}O$ during Heinrich events. When subtracting the Indian stalagmite $\delta^{18}O$ series from our XL15 record during H1 period, we found a significant negative correlation with sea surface temperature (SST) record of Western Pacific Warm Pool (WPWP). Consequently, our study suggests that the Chinese stalagmite $\delta^{18}O$ is controlled by both the ISM and EASM on orbital-, millennial-, and decadal timescales.

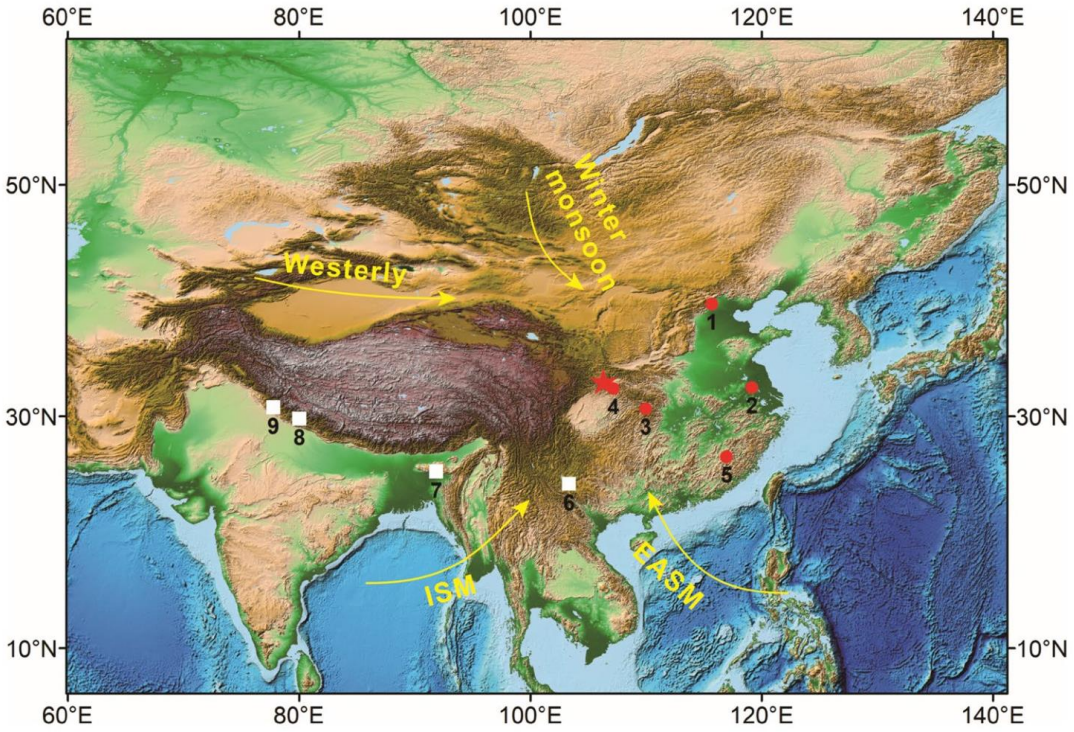

Figure 1. Location of Xianglong Cave (red fve-pointed star). Numbers indicate locations of the following caves: (1) Kulishu (Ma et al. 2012; Orland et al. 2015), (2) Hulu (Wang et al. 2001), (3) Haozhu (Zhang et al. 2016), (4) Songjia (Zhou et al. 2008), (5) Xianyun (Cui et al. 2017), (6) Xiaobailong (Cai et al. 2015; Tan et al. 2017), (7) Mawmluh (Dutt et al. 2015), (8) Timta (Sinha et al. 2005), (9) Bittoo (Kathayat et al. 2016). Yellow arrows indicate directions of the East Asian summer monsoon (EASM), Indian summer monsoon (ISM), East Asian winter monsoon, and westerly.

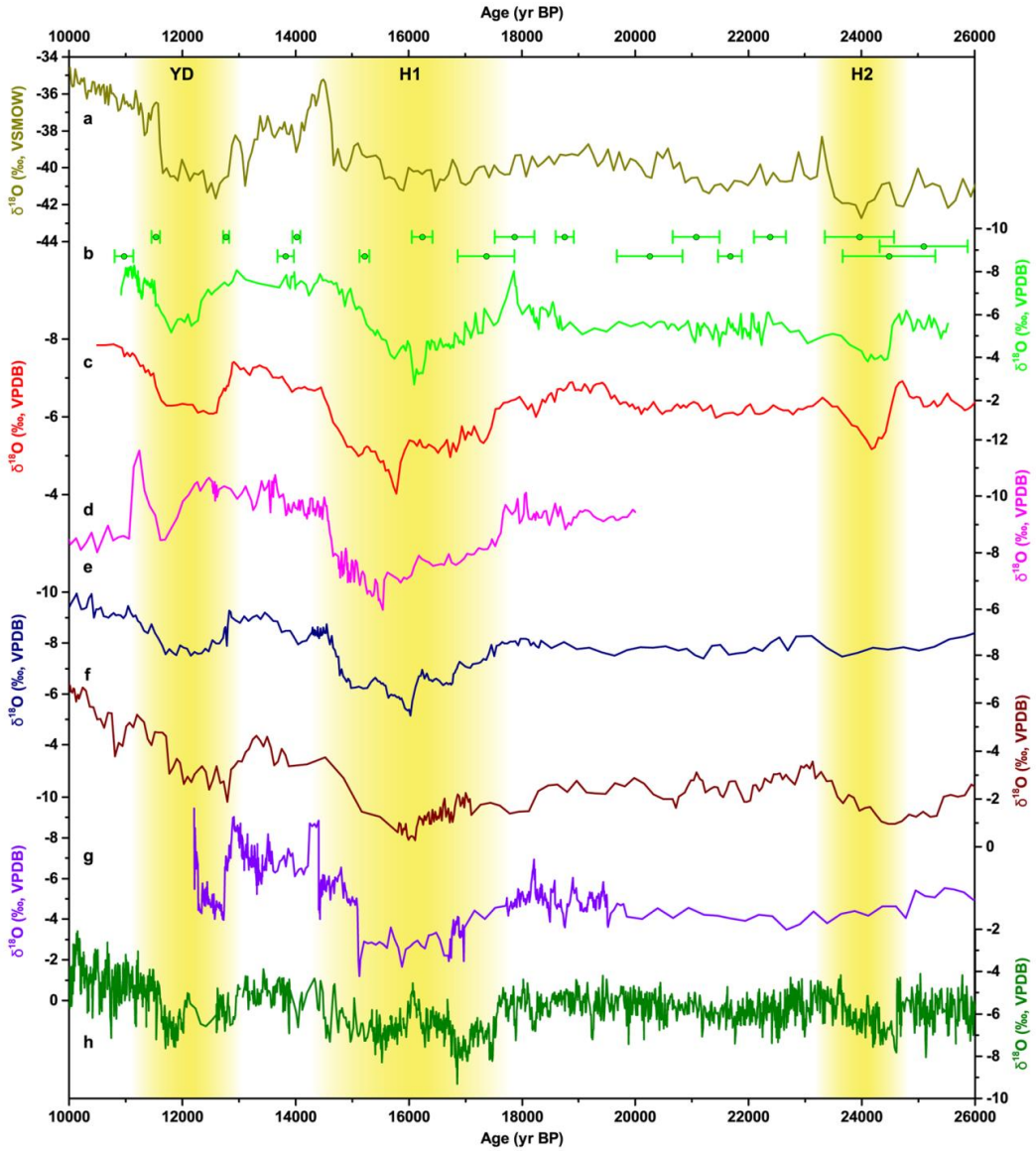

Figure 2. Comparison of XL15 $\delta^{18}O$ series with other records. a The $\delta^{18}O$ record of GISP2 (Grootes and Stuiver 1997). b XL15 $\delta^{18}O$ record. The age error bars (2σ) are color-coded by stalagmites. c The $\delta^{18}O$ record from Hulu Cave (Wang et al. 2001). d The $\delta^{18}O$ record of Songjia Cave (Zhou et al. 2008). e The $\delta^{18}O$ record of Haozhu Cave (Zhang et al. 2016). f The $\delta^{18}O$ record of Mawmluh Cave (Dutt et al. 2015). g The $\delta^{18}O$ record of Bittoo Cave (Kathayat et al. 2016). h The $\delta^{18}O$ record of Jaraguá Cave (Novello et al. 2017). The vertical yellow bars denote H2, H1, and YD events, respectively.

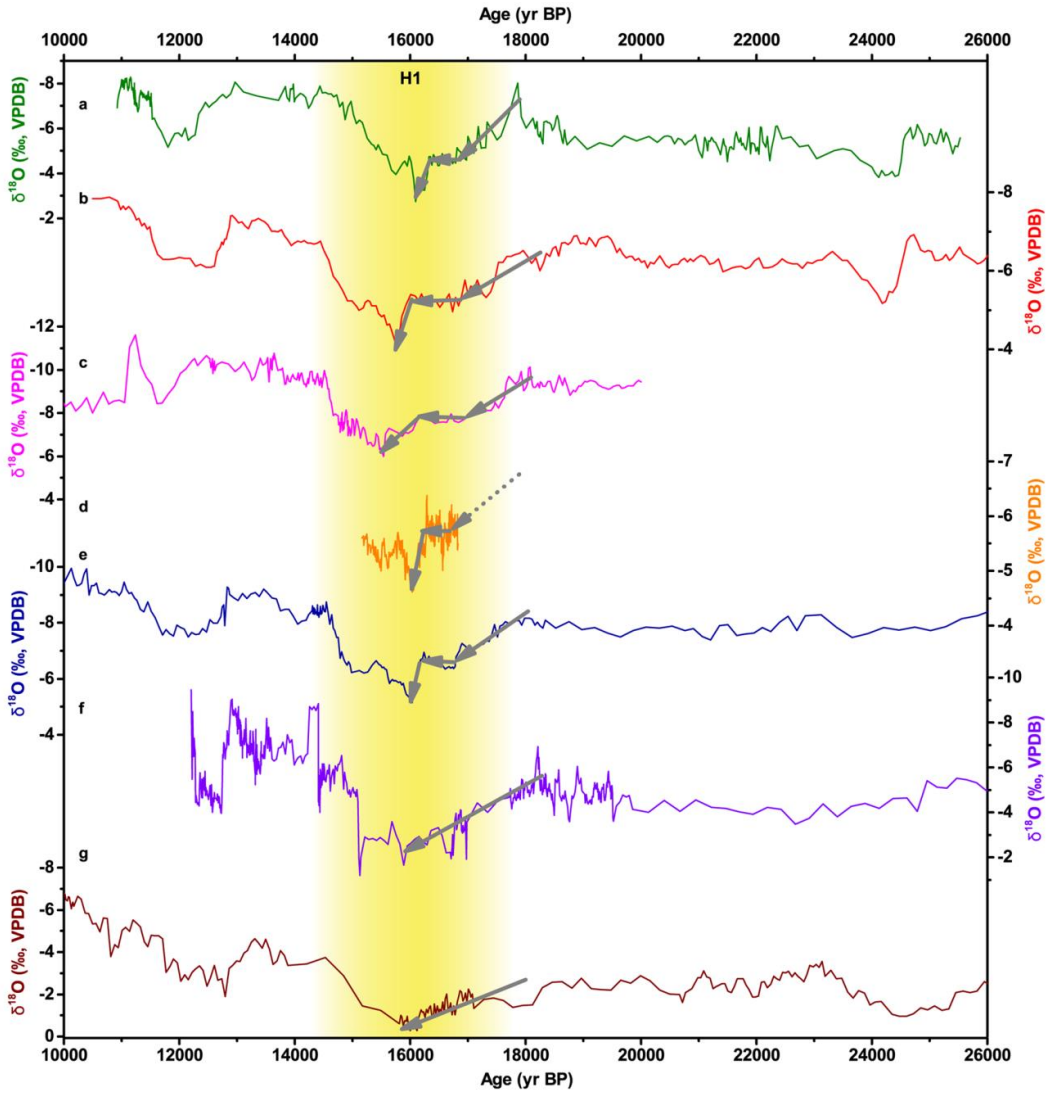

Figure 3. Comparison of mutation mode of H1 between a XL15, b Hulu (Wang et al. 2001), c Songjia (Zhou et al. 2008), d Xianyun (Cui et al. 2017), e Haozhu (Zhang et al. 2016), f Bittoo (Kathayat et al. 2016) and g Mawmluh (Dutt et al. 2015) cave records. The vertical yellow bar denotes H1 event.

7. 那不勒斯湾的磁学理论和应用：磁异常场与构造轮廓的关系

翻译人：曹伟 11930854@mail.sustech.edu.cn

Aiello G, Marsella E. ***Magnetic Theory and Applications in the Naples Bay (Southern Tyrrhenian Sea, Italy): Magnetic Anomaly Fields and Relationships with Morpho-Structural Lineaments****[J]. **World Journal of Condensed Matter Physics**, 2016, 6(3): 183-216.*

摘要：本文以意大利南部的那不勒斯湾为例，讨论了意大利南部复杂火山区的磁学理论和应用。本文已绘制了那不勒斯湾的磁异常图，目的是突出对 Eastern Tyrrhenian 边缘这一地区的地球物理学和火山学的新认识，它表现出复杂地球物理背景的特点，强烈依赖海底地形。文中讨论了海洋磁测和多波束测深的理论问题。磁数据处理包括日变校正、偏移校正以及数据水准测量做为函数进行的侧线交叉点校正。研究过程中参考了多波束和单波束测深数据处理，对那不勒斯湾的磁异常场进行了详细的地质解释，并且和通过形态测深法识别的主要形态特征构造进行对比。展示磁异常细节的导航测线选择与重要地震剖面相关联，它们包括索玛-维苏威火山杂岩附近的大陆架，弗雷格里安火山杂岩附近的火山口湾外陆架，五帕卢莫、尼西达和米塞诺的残余火山堤，那不勒斯斜坡上的盖亚火山堤，多恩峡谷的西斜坡，麦格纳基峡谷的顶部，伊斯基亚和前基达群岛之间的磁异常。

ABSTRACT：Magnetic theory and application to a complex volcanic area located in Southern Italy are here discussed showing the example of the Gulf of Naples, located at Southern Italy Tyrrhenian margin. A magnetic anomaly map of the Gulf of Naples has been constructed aimed at highlighting new knowledge on geophysics and volcanology of this area of the Eastern Tyrrhenian margin, characterized by a complex geophysical setting, strongly depending on sea bottom topography. The theoretical aspects of marine magnetometry and multibeam bathymetry have been discussed. Magnetic data processing included the correction of the data for the diurnal variation, the correction of the data for the offset and the leveling of the data as a function of the correction at the cross-points of the navigation lines. Multibeam and single-beam bathymetric data processing has been considered. Magnetic anomaly fields in the Naples Bay have been discussed through a detailed geological interpretation and correlated with main morpho-structural features recognized through morpho-bathymetric interpretation. Details of magnetic anomalies have been selected, represented

and correlated with significant seismic profiles, recorded on the same navigation lines of magnetometry. They include the continental shelf offshore the Somma-Vesuvius volcanic complex, the outer shelf of the Gulf of Pozzuoli offshore the Phlegrean Fields volcanic complex, the relict volcanic banks of Pentapalummo, Nisida and Miseno, the Gaia volcanic bank on the Naples slope, the western slope of the Dohrn canyon, the Magnaghi canyon's head and the magnetic anomalies among the Ischia and Procida islands.

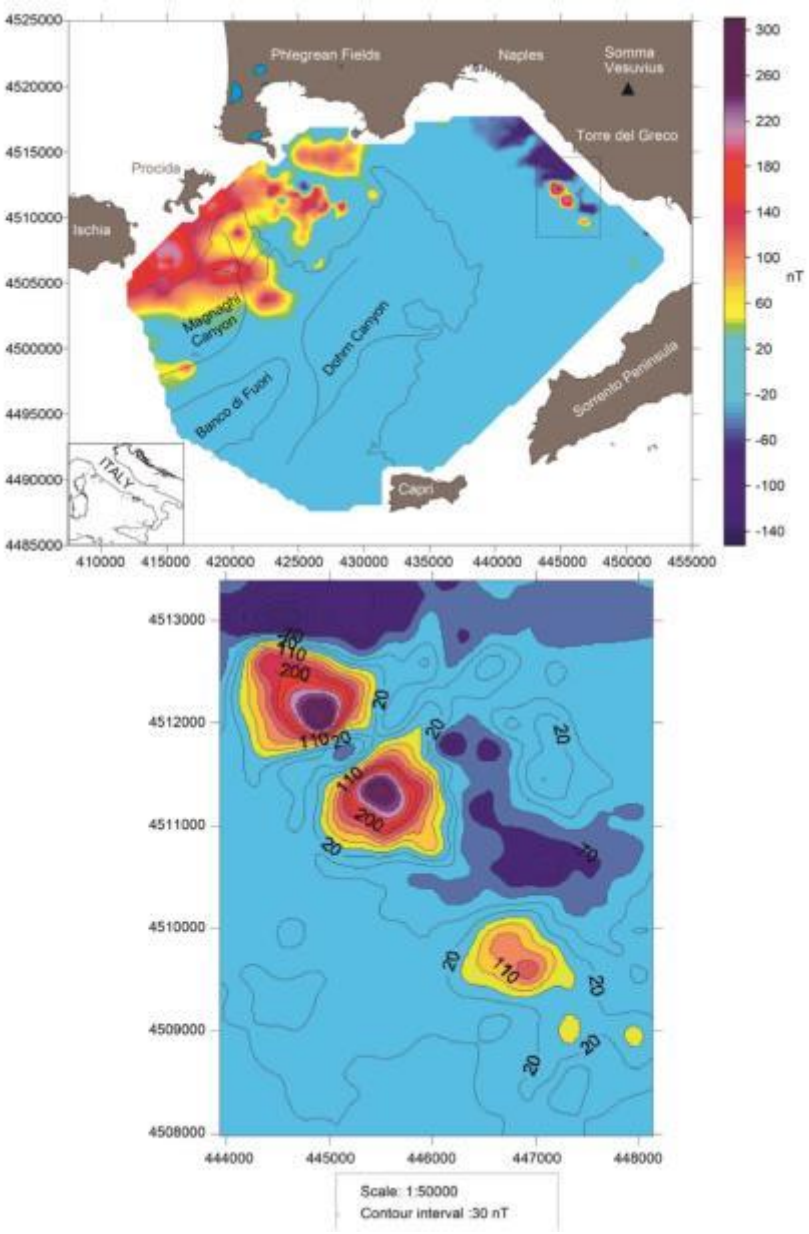

Figure 1. Detailed magnetic anomaly field map offshore the Somma-Vesuvius volcanic complex (on the bottom) and location on the magnetic anomaly field map (on the top).

8. 重构末次冰期以来湄公河流域的化学风化强度

翻译人：王浩森 502691781@qq.com

Jiwarungrueangkul T, Liu Z, Stattegger K, et al. ***2019. Reconstructing Chemical Weathering Intensity in the Mekong River Basin Since the Last Glacial Maximum. 34: 1710-1725.***

摘要：本文研究了南海南部湄公河口外SO18383-3高分辨率岩芯的粘土矿物学和主要地球化学元素指标，以重建自上次冰期以来的沉积物来源和化学风化强度。年代表是基于有孔虫利用加速器质谱仪得到的^{14}C的日期。粘土矿物分析表明，湄公河是该研究地区的主要沉积源。化学变化指数（CIA）的值表明湄公河流域的化学风化程度中等。蒙脱石/（伊利石+绿泥石）和蒙脱石/高岭石的比率与TiO_2/K_2O的比值同时揭示了湄公河流域化学风化强度的随时间变化。末次冰期最大值（29.9－14.7 cal ka BP），Heinrich事件1（∽14.8 cal ka BP），新仙女木时期（12.4－11.3 cal ka BP）和中新世晚期（7.6－ 1.1 cal ka BP）结果表明化学风化强度较弱。相反的，在Bølling-Allerød时期（14.7-12.7 cal ka BP）和主要冰消期（14.7-7.6 cal ka BP）期间的比值较高，表明湄公河流域的化学风化更强。这些记录与东亚夏季风强度的记录之间的良好相关性表明，最近30 ka湄公河流域的化学风化强度主要受夏季风的控制。这项研究极大地加深了我们对自上次冰河极大期以来湄公河流域大陆风化的主要强迫因素的认识。

ABSTRACT：High-resolution clay mineralogy and major element geochemistry of Core SO18383-3 collected off the Mekong River mouth in the southern South China Sea have been investigated, aiming to reconstruct sediment provenance and chemical weathering intensity since the last glaciation. The chronology is based on foraminiferal accelerator mass spectrometry ^{14}C dates. Clay mineral analysis suggests that the Mekong River is a major sedimentary source for the studied area. The values of chemical index of alteration (CIA) indicate moderate chemical weathering in the Mekong River basin. Smectite/(illite + chlorite) and smectite/kaolinite ratios coupled with TiO_2/K_2O ratio reveal the temporal variation in chemical weathering intensity in the Mekong River basin. The lower ratios around the Last Glacial Maximum (29.9–14.7 cal ka BP), the Heinrich Event 1 (~14.8 cal ka BP), the Younger Dryas interval (12.4–11.3 cal ka BP), and middle to late Holocene (7.6–1.1 cal ka BP) indicate weak chemical weathering intensity. In contrast, the higher ratios occurring during the Bølling-Allerød period (14.7–12.7 cal ka BP) and the period of main deglaciation (14.7–

7.6 cal ka BP) indicate stronger chemical weathering in the Mekong River basin. The good correlations between these proxies and the available proxy records of the East Asian summer monsoon intensity suggest that the intensity of chemical weathering in the Mekong River basin over the last 30 ka is significantly controlled by the summer monsoon. This study greatly increases our understanding of the principal forcing factor on continental weathering in the Mekong River basin since the Last Glacial Maximum..

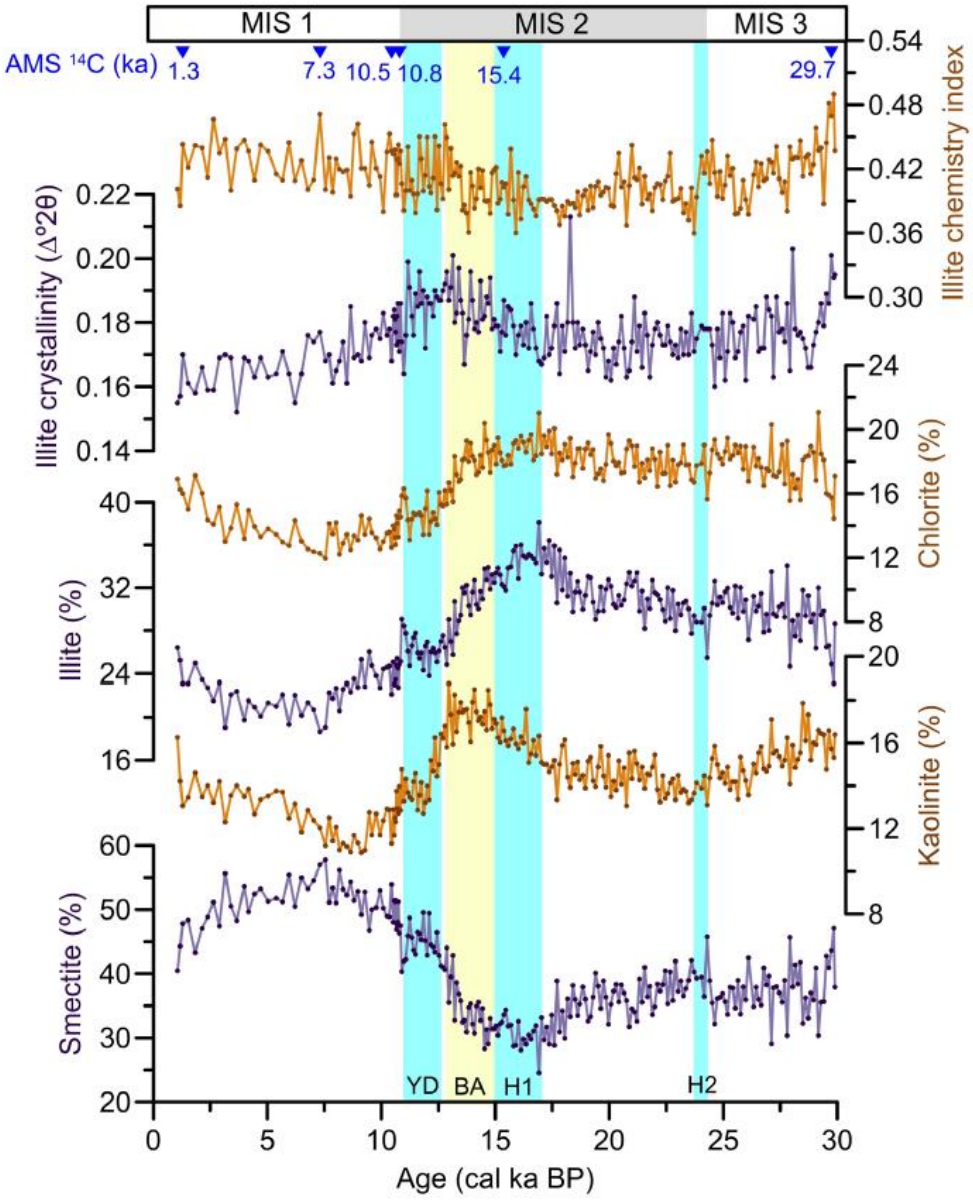

Figure 1. Temporal variations in clay mineral assemblage of Core SO18383- 3. The foraminiferal accelerator mass spectrometry (AMS) ^{14}C datings (blue triangle) is also displayed. The shaded bars indicate Heinrich Events (H1 and H2), Bølling-Allerød (BA), and the Younger Dryas (YD; Wang et al., 2001).

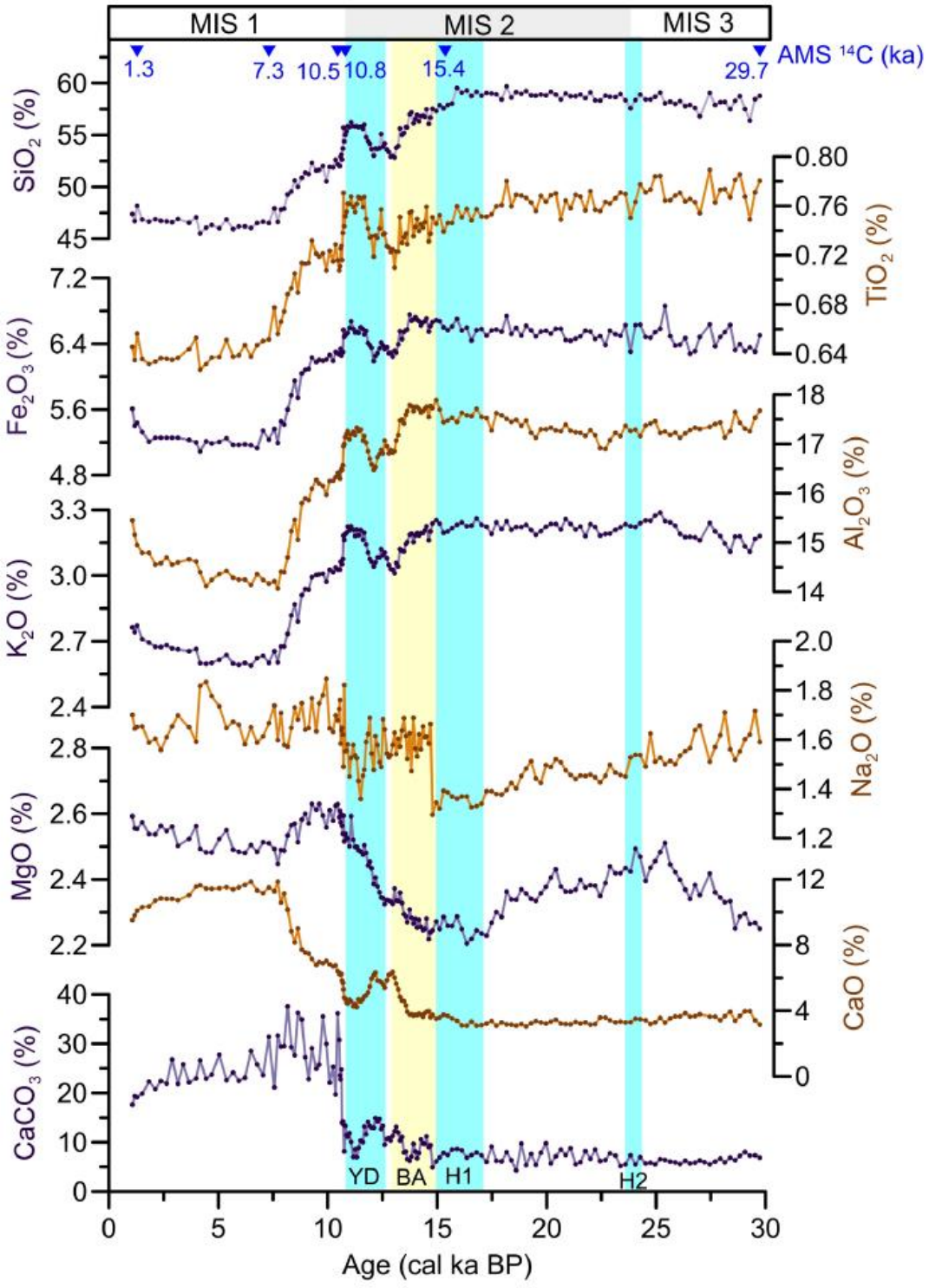

Figure 2. Temporal variations in major element contents of Core SO18383- 3. The foraminiferal accelerator mass spectrometry (AMS) ^{14}C datings (blue triangle) is also displayed. Carbonate content ($CaCO_3$%) shows a linear correlation to CaO (%). The shaded bars indicate abrupt climate events as in

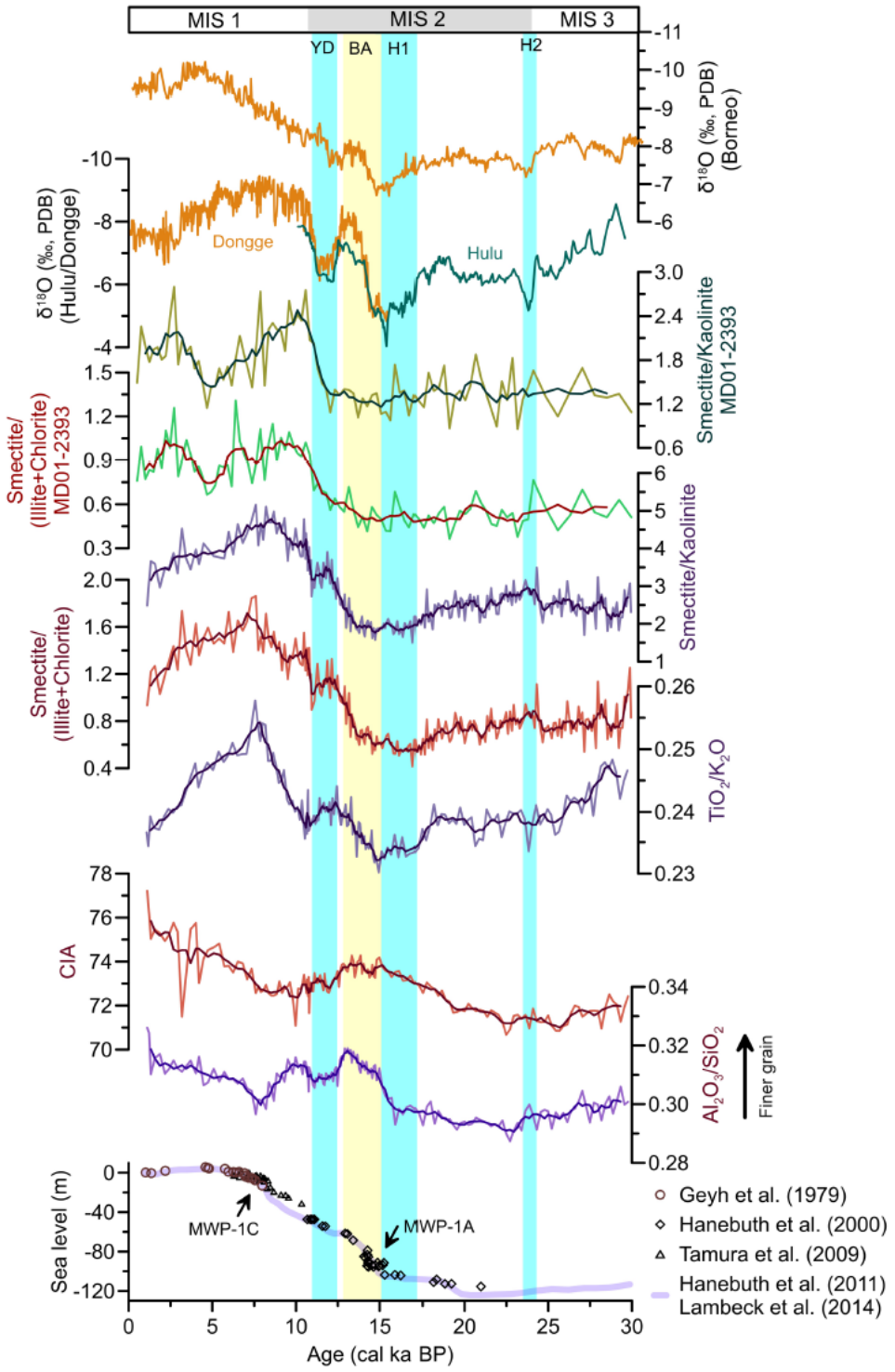

Figure 3. Temporal variations of chemical weathering proxies of Core SO18383-3 since the Last Glacial Maximum and comparison with stalagmite $\delta^{18}O$ of Dongge, Hulu, and northern Borneo Caves from Wang et al. (2001), Dykoski et al. (2005), and Carolin et al. (2016). Clay mineral ratios of Core MD01-2393 are from Liu et al. (2004). Sea level data are from Geyh et al. (1979), Hanebuth et al. (2000, 2011), Tamura et al. (2009), and Lambeck et al. (2014). All parameters of Core SO18383-3 are smoothed with a five-point running average to obtain more general trends. The shaded bars indicate abrupt climate events as in Figure 1.

9. Acycle：用于古气候研究和教育的时间序列分析软件

翻译人：郑威 11930589@mail.sustech.edu.cn

Li M, Hinnov L, Kump L. ***Acycle: Time-series analysis software for paleoclimate research and education****[J].* ***Computers & geosciences****, 2019, 127: 12-22.*

摘要：识别和解释沉积物代用指标数据指示的古气候信号耗时且主观。Acycle是一个全面且易于使用的用于古气候研究和教育的时间序列分析的软件包。它旨在加速古气候时间序列分析，特别是旋回地层学，并且提供客观方法用于估计天文学因素。Acycle提供了多种消除趋势选项用于追踪和去除长期趋势，提供了多种功率谱分析方法用于检测周期信号。许多专用于旋回地层学和天文学的功能不在标准统计包中。该软件提供了功能专门用于评估天文（米兰科维奇）驱动的古气候序列和通过评估天文解的能谱与沉积物代用指标数据间的相关系数寻找最适合的沉积速率。Acycle还提供了沉积物噪声建模（用于古海平面变化）。例如，Acycle被用于一个来自于Svalbard古近纪中央盆地的BH9/05岩心的古新世-始新世极热期（PETM）旋回地层的沉积物代用指标序列。在PETM期间和之后，Acycle在代用指标序列中检测到显著的天文强迫和相对稳定的沉积速率。Acycle是一个开源软件，在MATLAB环境中运行，或作为独立软件在Windows和Macintosh OS X上运行。

ABSTRACT：Recognition and interpretation of paleoclimate signals in sedimentary proxy datasets are time consuming and subjective. Acycle is a comprehensive and easy-to-use software package for time series analysis in paleoclimate research and education. It is designed to speed paleoclimate time series analysis, especially cyclostratigraphy, and to provide objective methods for estimating astrochronology. Acycle provides for detrending with multiple options to track and remove secular trends. A selection of power spectral analysis methodologies is offered for the detection of periodic signals. Many of the functions are specific to cyclostratigraphy and astrochronology that are not found in standard statistical packages. A specialized function is provided to assess the astronomical (Milankovitch) forcing of paleoclimate series and search for the most likely sedimentation rate by evaluating the correlation coefficient between power spectra of an astronomical solution and sedimentary proxy data. Sedimentary noise modeling (for past sea-level changes) is also provided in Acycle. As an example, Acycle is applied to a sedimentary proxy series from the cyclostratigraphy of the Paleocene-Eocene thermal maximum (PETM) in Core BH9/05 from the Paleogene Central

Basin, Svalbard. Acycle detects significant astronomical forcing in the proxy series and relatively stable sedimentation rates during and after the PETM. Acycle runs in the MATLAB environment or as stand-alone software on Windows and Macintosh OS X, and is open-source software.

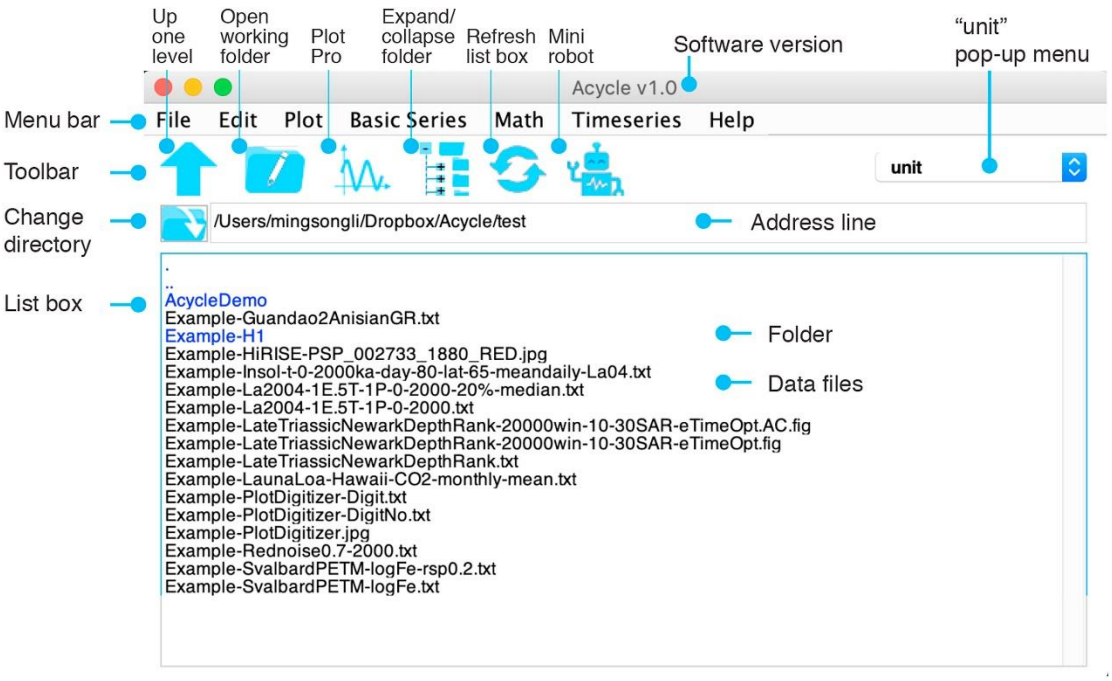

Figure 1. *Acycle* graphical user interface (GUI).